



Effects of Ga Content on Dynamic Recrystallization and Mechanical Properties of High Strain Rate Rolled Mg–Ga Alloys

Wensen Huang^{1,2} · Jihua Chen^{1,2} · Hongge Yan^{1,2} · Weijun Xia^{1,2} · Bin Su^{1,2} · Weijun Zhu¹

Received: 17 April 2019 / Accepted: 3 July 2019 / Published online: 22 July 2019
© The Korean Institute of Metals and Materials 2019

Abstract

The Mg–*x*Ga (*x* = 1, 2, 3 and 5 in mass%) alloys are subjected to high strain rate rolling (HSRR) at 275 °C with the rolling strain rate of 9.1 s⁻¹ to develop high performance Mg alloy sheets with high plasticity. Effects of Ga content on microstructure and mechanical properties of the Mg–Ga alloys are investigated by SEM, XRD, tensile testing and etc. The Ga addition can reduce the critical strain of DRX in Mg alloys, which is associated with the reduced stacking fault energy, the increased twinning density during deformation and the more DRX nucleation sites during HSRR. With the Ga content increasing from 2 to 3%, the reduced DRX degree is attributable to the hindrance of dynamic precipitates. With the Ga content increasing from 3 to 5%, the slightly increased DRX degree can be ascribed to the relatively coarse precipitates. The Mg–2 Ga alloy sheet, featured with complete DRX, exhibits an ultra-high plasticity (with the elongation to rupture of 36.6%) and a relatively low anisotropy of yield strength and plasticity. The Mg–5 Ga alloy sheet has the best comprehensive mechanical properties, with the ultimate tensile strength of 292 MPa, yield strength of 230 MPa and elongation to rupture of 30.3%, which can be ascribed to the combination of grain refinement strengthening and precipitation strengthening.

Keywords Mg–Ga alloy · Dynamic recrystallization · High strain rate rolling · High plasticity

1 Introduction

Magnesium alloys are being increasingly evaluated for their applications in aerospace, automotive industry and electronic components because of their high specific strength,

low density and excellent machinability [1–3]. However, their extensive applications are limited due to their poor formability and insufficient strength at room temperature. Most of magnesium alloys have a hexagonal close-packed (HCP) crystal structure which contains a limited slip systems and a large discrepancy of critical resolved shear stress (CRSS), especially at RT [4, 5], which results a poor formability. The methods for strength improvement such as alloying, severe plastic deformation (SPD) and so on are developed in the previous studies. Recently, wrought Mg alloys have attracted more and more attentions since hot working can improve the workability, modify the final microstructure and enhance the related mechanical properties. No doubt, DRX plays a significant role in the thermo-mechanical processing. It is reported that DRX can also be reinforced by the addition of alloying elements during the various thermo-mechanical processes [6]. There are two forms of alloying elements existed in Mg alloys. One is the solid solute state, which can affect the DRX process by increasing or decreasing the stacking fault energy (SFE) [7, 8]. The other is the inter-metallic state, which can obstruct or promote the DRX process [9, 10]. Therefore, it is of great significance to study the effects of alloying elements on DRX in Mg alloys.

✉ Jihua Chen
jihua.chen2005@163.com

✉ Hongge Yan
yanhg68@163.com

Wensen Huang
576706034@qq.com

Weijun Xia
xwjyxbyy@sina.com

Bin Su
subindier2008@126.com

Weijun Zhu
324246117@qq.com

¹ School of Materials Science and Engineering, Hunan University, Changsha 410082, China

² Hunan Provincial Key Laboratory of Spray Deposition Technology & Application, Hunan University, Changsha 410082, China

Gallium (Ga) is an interesting novel alloying element, which has attracted more attentions in the field of functional materials. Most research works are focused on the Mg–Ga phase diagram [11–14]. Some studies are conducted on the Mg–Ga alloys as the sacrificial anodes in seawater batteries [15–17] and for hydrogen storage [18]. The Ga addition can promote the electrochemical activity of Mg due to the faster dissolution of Mg anode in the environment containing the aggressive ions [19, 20]. In particular, the activation of α -Mg is associated with the presence of the secondary phases ($\text{Mg}_{21}\text{Ga}_5\text{Hg}_3$ and Mg_5Ga_2) inducing the electrochemical activity and the dissolution re-deposition process in the Mg–Ga–Hg system [21, 22]. Some studies are conducted on the as-cast Mg–Ga alloy for the biomedical applications [23–25], which shows an acceptable corrosion resistance in 0.9 wt% NaCl and low toxicity.

In recent years, a few studies have been conducted on the mechanical properties of the as-cast Mg–Ga alloys [24, 25]. Liu et al. have found that Ga has a distinct solid solution strengthening effect and the Mg–Ga alloy exhibits an obvious age hardening effect [26]. Moreover, the Ga addition can reduce the axial ratio (c/a) and the stacking fault energy of Mg [27–29]. However, almost no studies on wrought Mg–Ga alloys have been reported till now. According to our preliminary experimental results, the Mg–Ga alloy system has a great potential in developing wrought Mg alloy sheets with an ultra-high plasticity and will find extensive applications in industries. In view of the high solid solubility of Ga in Mg, the possible formation of the intermetallics with Mg and the enhanced DRX effect of HSRR [30], effects of Ga content on DRX and mechanical properties of the HSRRed Mg–Ga alloys are carefully studied. The aim of this work is to provide a better understanding of the effects of Ga content on DRX and mechanical properties of the HSRRed Mg–Ga alloys, as well as to offer the possible underlying method controlling the microstructure, which will lay foundations for developing the wrought Mg alloy sheets suitable for punch forming and super-plastic forming.

2 Experimental Details

The binary Mg–Ga alloy ingots were prepared with commercial high-purity Mg (> 99.9%) and Ga (> 99.99%) as the raw materials. The alloys were melted in an electric resistance furnace with a mild steel crucible protected by the RJ-2 flux [37.1% KCl + 4.8% CaF_2 + 43.2% MgCl_2 + 6.8% BaCl_2 + 6.6% (NaCl + CaCl_2) + 1.3% water-insoluble – 0.4% moisture]. The melt was purged at 780 °C for 10 min and held at 760 °C for 15 min, so that homogenization of alloying elements and settlement of inclusions could be realized. Then molten alloys were cast into a steel mould (150 mm × 100 mm × 20 mm) at 720 °C. The actual chemical

compositions of the experimental alloys were determined by the X-ray fluorescence spectrometry, which were listed in Table 1. Hereafter, the Mg–Ga alloys were referred as Mg–1 Ga, Mg–2 Ga, Mg–3 Ga and Mg–5 Ga, respectively. The as-cast ingots were solution treated at 375 °C for different intervals from 10 to 12 h.

The solution treated ingots were machined to the initial size of 90 mm in length, 60 mm in width and 10 mm in thickness (H) for HSRR. The 360 mm × 600 mm double roller mill with the speed of 430 mm s^{-1} was adopted. The billets were pre-heated to 275 °C for 13 min before rolling while the rolls were not heated. The pre-heated billets were rolled by a single pass to the final thickness of 2 mm (h) with the reduction (λ) of 80% and the corresponding average strain rate ($\dot{\epsilon}$) was 9.1 s^{-1} . $\dot{\epsilon}$ was calculated by the equation $\dot{\epsilon} = \frac{H-h}{H} \frac{V}{\sqrt{R(H-h)}}$ (see Ref. [30] for detail), where V was the roll circumferential speed (430 mm s^{-1}) and R was the roller radius (180 mm). Cylindrical samples (ϕ 8 mm × 10 mm) machined from the solution treated ingots were adopted for hot compression and hot compression testing was conducted on a Gleeble-3500 thermo-mechanical machine at 275 °C, with the strain rate of 9.1 s^{-1} and the maximum true strain of 1.61. The specimens were heated to 275 °C at a heating rate of 9 °C s^{-1} and held for 13 min before hot compression. The hot-compressed samples were quenched immediately in water to preserve the as-deformed microstructures.

The microstructures were observed by a MM-6 metallographic microscope (OM) after etching with a solution of 0.3 g oxalic acid, 1 ml acetic acid, 1.5 ml water and 10 ml ethanol. The average grain size was measured by the intercept method and the average DRX volume fraction was calculated using the Image-Pro Plus 6.0 software. The overall phase constitutions of the as-studied alloys were analyzed by a D5000 X-ray diffraction (XRD) instrument with Cu $K\alpha$ at a scanning rate of 0.1 ° s^{-1} . The HSRRed plates were machined into the flat tensile specimens along the rolling direction (RD) with the gauge size of 55 mm × 4 mm × 2 mm. In addition, the tensile specimens were also sectioned from the as-rolled Mg–2 Ga alloy sheet along 45° to rolling direction (RD-45°) and transverse direction (TD). Tensile testing was conducted on an Instron 3369 tensile testing machine with the initial strain rate of $1.1 \times 10^{-3} \text{ s}^{-1}$ at room temperature. Ultimate tensile strength (σ_b), yield tensile strength ($\sigma_{0.2}$) and elongation to rupture (δ) were averaged over three specimens. Fractographic observations were conducted on a FEI

Table 1 The chemical compositions of the Mg–Ga alloys (mass%)

Alloys	Mg–1 Ga	Mg–2 Ga	Mg–3 Ga	Mg–5 Ga
Nominal Ga content	1	2	3	5
Actual Ga content	0.9	1.8	2.6	4.6

QUANTA 200 scanning electron microscopy (SEM). The micro-compositional analysis of some certain phases was conducted on a FEI QUANTA 200 SEM equipped with the Oxford X-ray energy dispersive spectroscopy (EDS).

3 Results

3.1 As-solutionized Microstructure

According to the binary Mg–Ga phase diagram [12], the eutectic reaction ($L \rightarrow \alpha\text{-Mg} + \text{Mg}_5\text{Ga}_2$) occurs at 422.7 °C and the solid solubility of Ga in Mg increases with the lower temperature. The Mg_5Ga_2 phase particles can be precipitated from the supersaturated $\alpha\text{-Mg}$ solid solution and thus the as-cast Mg–Ga alloys contain $\alpha\text{-Mg}$ and Mg_5Ga_2 . In order to improve the plastic working properties, the removal of the secondary phase particles by homogenization is desirable in the Mg–Ga alloys before hot deformation. The as-solutionized microstructures of the Mg–Ga alloys are shown in Fig. 1. The grain size of the alloy becomes smaller with the higher Ga content, indicating the significant grain-refining effect of Ga on Mg alloys, which is in good consistency

with the study of Marta Mohedano [23]. Grain boundaries become slender and straight after solution treatment and almost no secondary phases are detected. The XRD pattern of the as-solutionized Mg–5 Ga alloy is shown in Fig. 2.

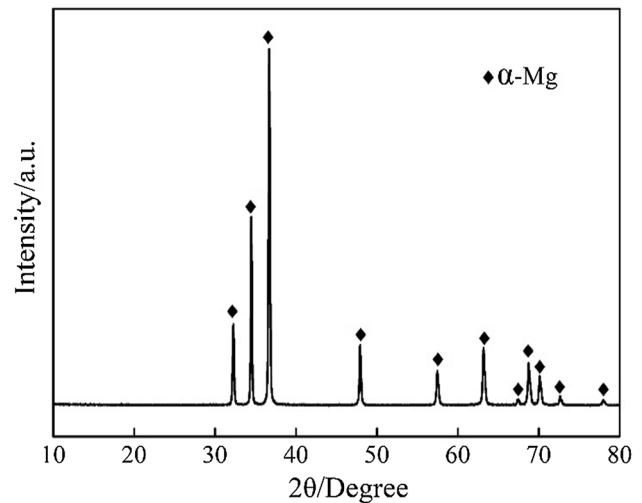


Fig. 2 XRD pattern of the as-solutionized Mg–5 Ga alloy

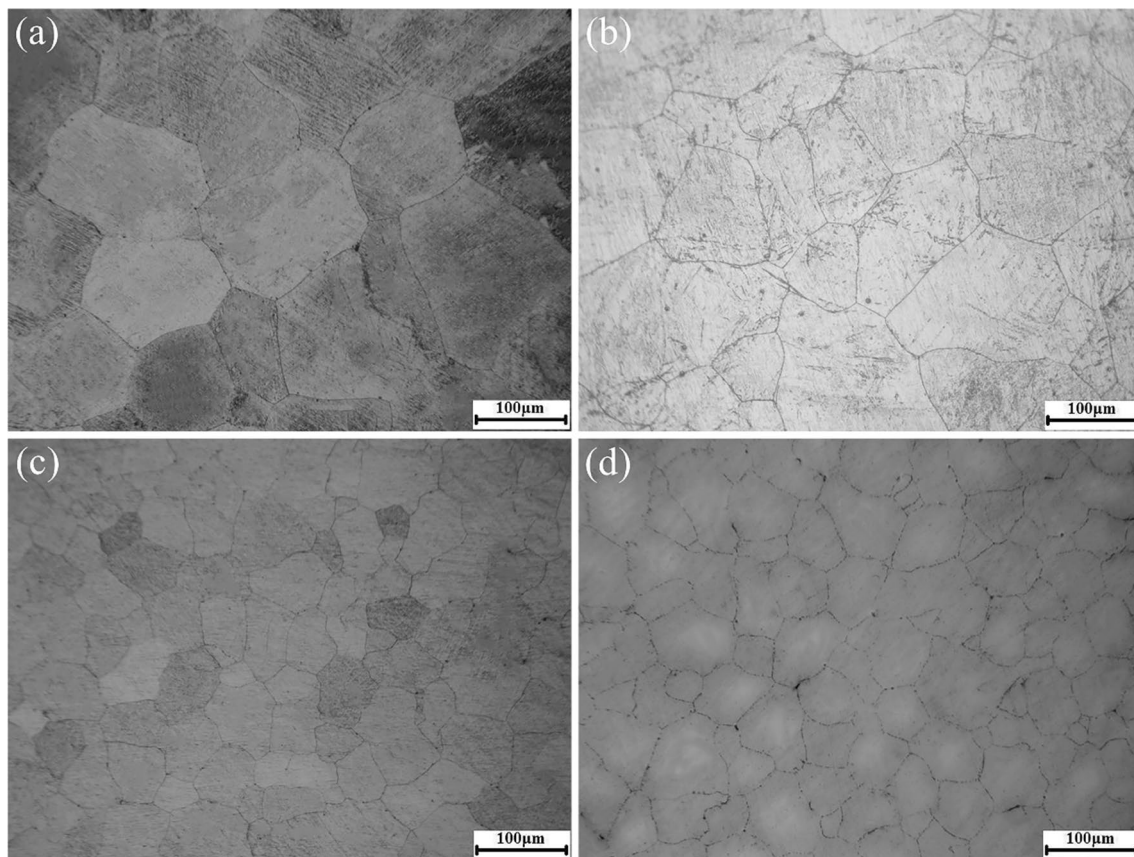


Fig. 1 OM images of the as-solutionized **a** Mg–1 Ga, **b** Mg–2 Ga, **c** Mg–3 Ga, and **d** Mg–5 Ga alloys

Only the α -Mg phase is detected and the secondary phase is completely dissolved in the matrix.

3.2 As-rolled Microstructure

The surface layer microstructures of as-rolled Mg–Ga alloys are shown in Fig. 3. As seen from Fig. 3a, c and d, DRX occurs in all the alloys and some un-DRX regions (indicated by arrows) are detected. As seen from Fig. 3b, no un-DRX region is detected in the Mg–2 Ga alloy. Obviously, the Ga content has an evident effect on the microstructure evolution.

As shown in Fig. 4, both the DRX volume fraction and the DRX grain size increase at first and then decrease with a higher Ga content. The DRX volume fraction of the alloy increases from 86 to 98% with the Ga content from 1 to 2% and then slightly decreases. The DRX grain size of the alloy increases from 2.4 to 2.8 μm with the Ga content from 1 to 3% and then slightly decreases.

The central layer microstructures of as-rolled Mg–Ga alloys are shown in Fig. 5. In consistency with our previous results [30], twins and twin-induced recrystallization can be found in the Mg–1 Ga and Mg–2 Ga alloys, while it is completely recrystallized in the Mg–3 Ga and Mg–5 Ga

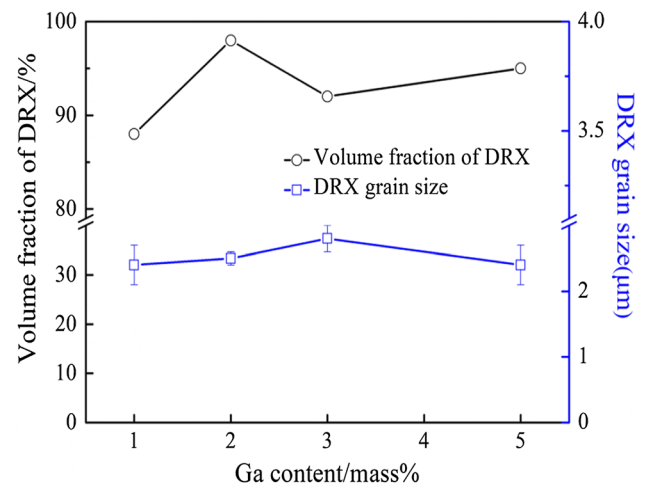


Fig. 4 The changes of the DRX grain size and the DRX volume fraction with the Ga content

alloys. A careful comparison between Fig. 5a and b shows that the DRX degree of Mg–1 Ga alloy is far less than that of Mg–2 Ga alloy and both the number and the density of twins in the Mg–1 Ga alloy are less than that the counterparts in

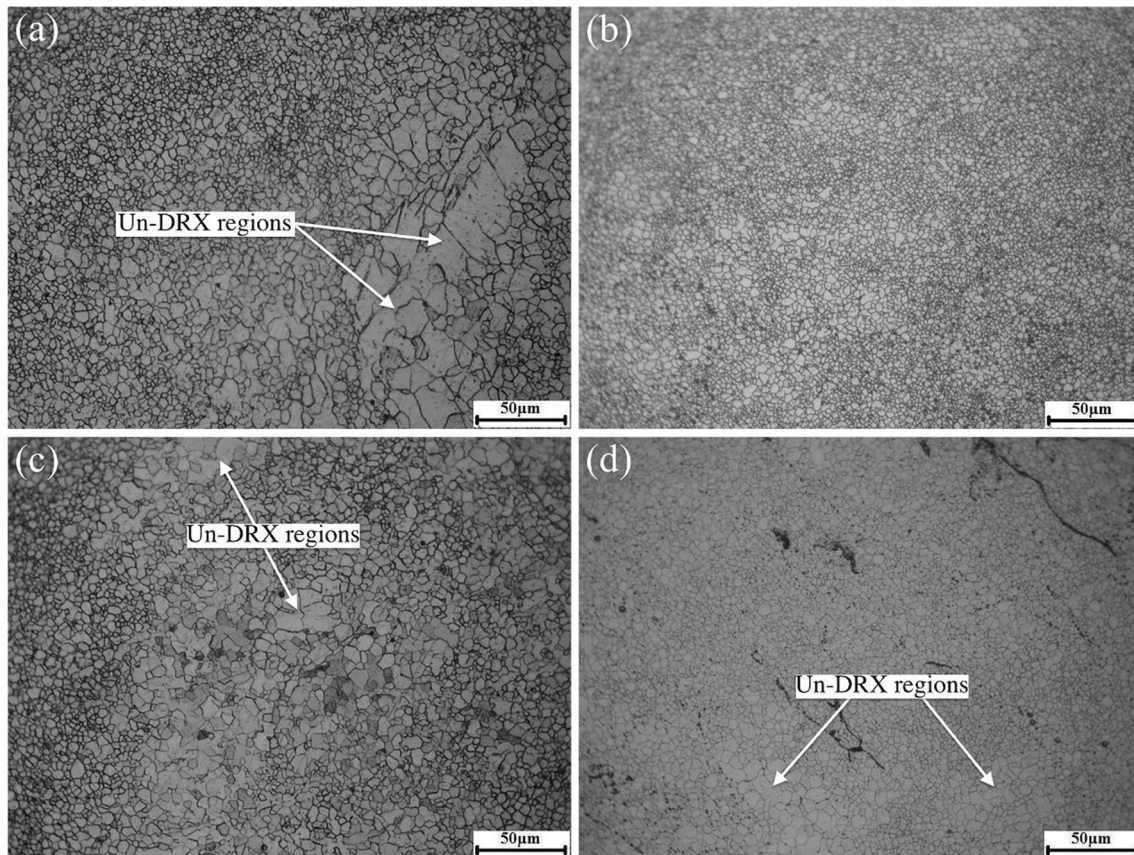


Fig. 3 OM images of the as-rolled **a** Mg–1 Ga, **b** Mg–2 Ga, **c** Mg–3 Ga, and **d** Mg–5 Ga alloys (surface)

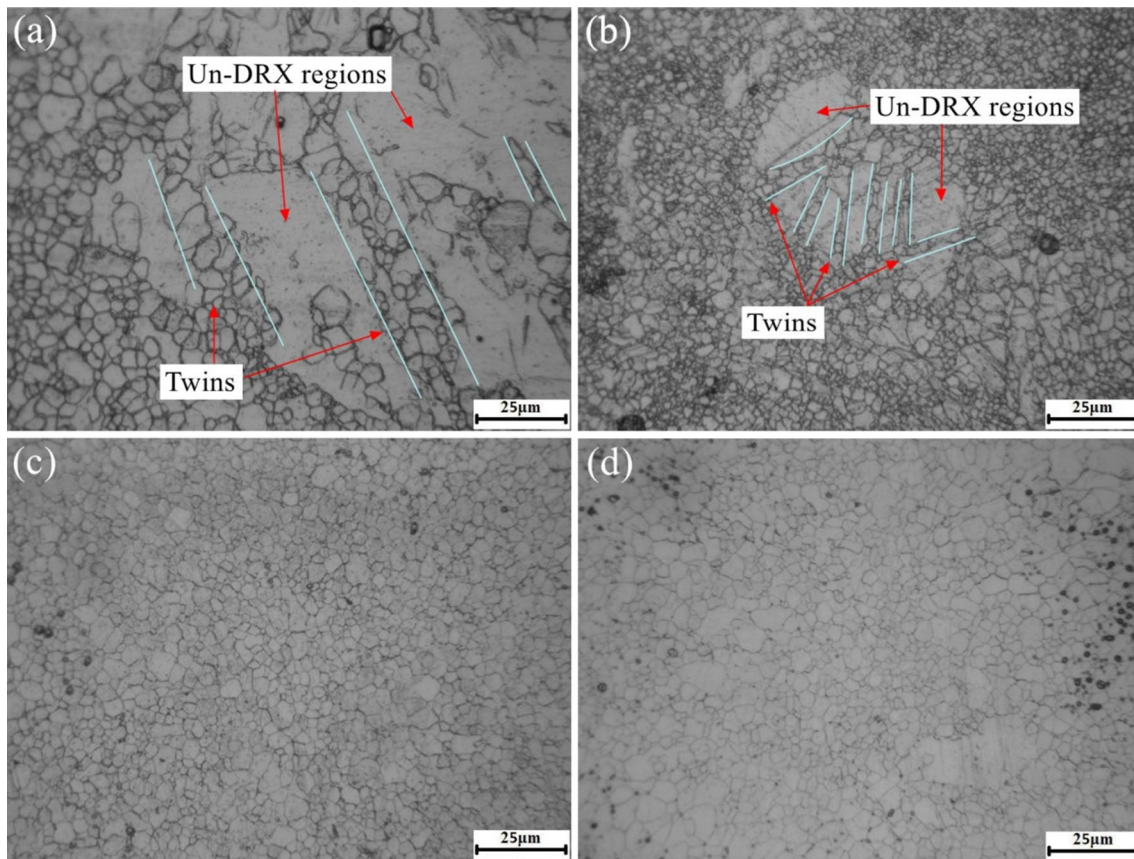


Fig. 5 OM images of the as-rolled **a** Mg–1 Ga, **b** Mg–2 Ga, **c** Mg–3 Ga, and **d** Mg–5 Ga alloys (central)

Mg–2 Ga alloy. The latter means that the increase of Ga content can increase the number of twins generated in the deformation process. Therefore, it can be inferred that the reason for the different DRX degree of the alloy with different Ga content is related to the degree of twins-induced recrystallization. As for the Mg–3 Ga and Mg–5 Ga alloys (Fig. 5c and d), both the center layer and the surface layer are featured with complete DRX, indicating that the increase of Ga content can enhance the microstructural homogeneity of the as-rolled plate.

The XRD patterns of the as-rolled Mg–Ga alloys are shown in Fig. 6. The visible Mg_5Ga_2 diffraction peaks are detected and their intensities increase with a higher Ga content. The Mg_5Ga_2 phase is possibly precipitated from α -Mg during HSRR since no Mg_5Ga_2 phase is detected in the as-solutionized Mg–5 Ga alloy.

3.3 Effects of Ga Content on the Critical Strain of DRX

In order to further study the effects of Ga content on the DRX behavior of the Mg–Ga alloys during the high strain rate deformation, hot compression testing at 275°C with

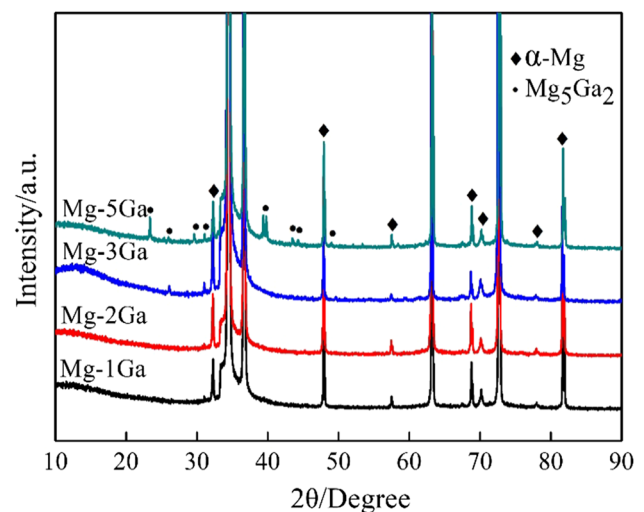


Fig. 6 XRD patterns of the as-rolled Mg–Ga alloys

the strain rate of 9.1 s^{-1} and the true strain of 1.61 is conducted. The typical true stress-true strain curves are shown in Fig. 7a.

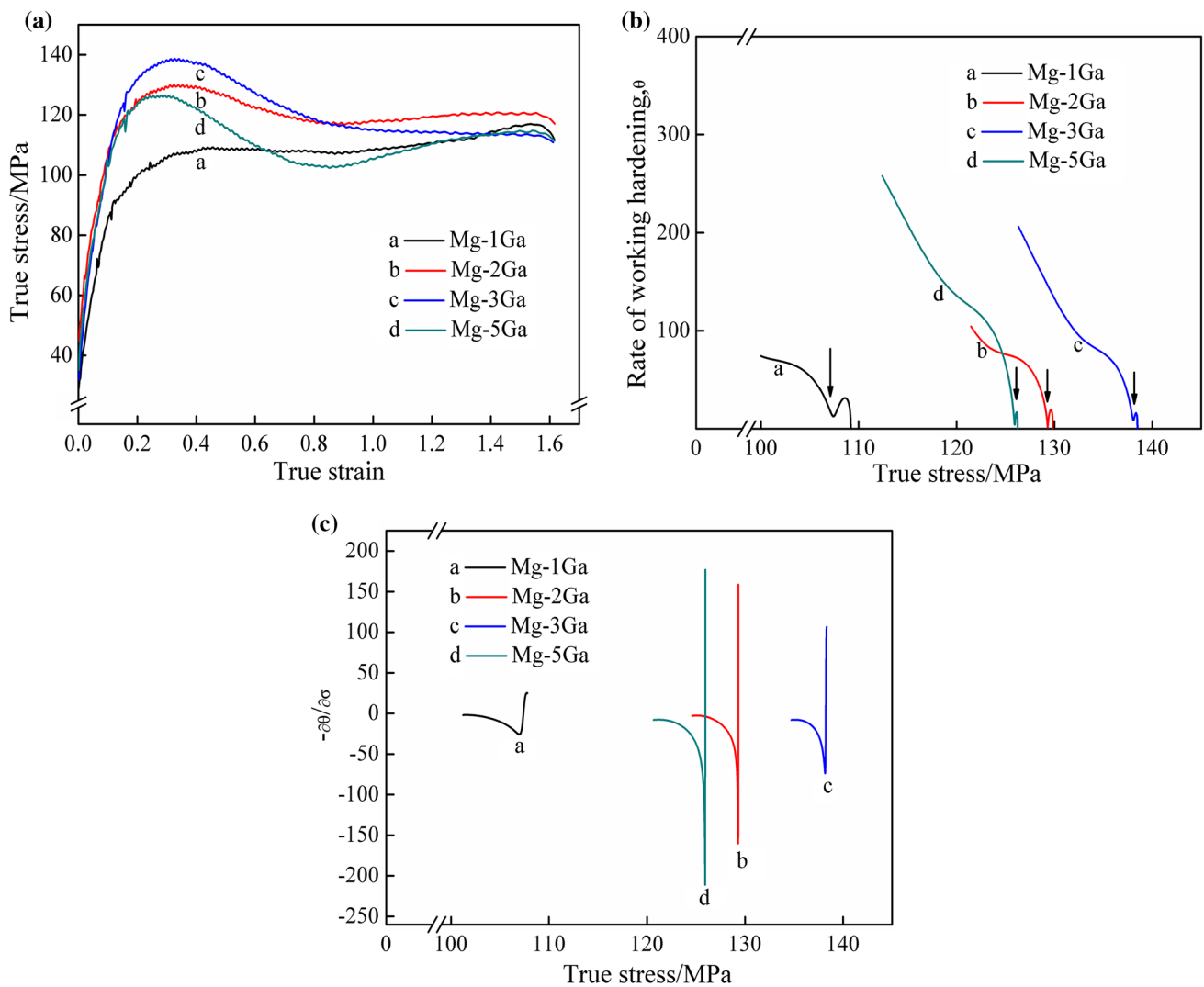


Fig. 7 The typical true stress–strain curves obtained by hot compression (a), θ – σ (b) and $-\partial\theta/\partial\sigma$ – σ (c) curves of the Mg–Ga alloys

Table 2 The peak stress and the peak strain of the Mg–Ga alloys

Ga content (mass%)	Peak stress σ_p (MPa)	Peak strain ε_p
1	109	0.438
2	130	0.339
3	139	0.341
5	127	0.293

The peak stress (σ_p) and peak strain (ε_p) of the Mg–Ga alloys are listed in Table 2. Clearly, the Ga content has a significant effect on the rheological behavior. As seen from Table 2, σ_p increases at first and then decreases with the higher Ga content, and the highest σ_p value is reached with 3% Ga. The increase in σ_p can be attributed to the solid solution strengthening of Ga [24, 25], while the reduced σ_p value of Mg–5 Ga is possibly associated with the reduction

of the axial ratio of α -Mg. The reduction of axial ratio can promote the initiation of the non-basal slip, which is beneficial to the dynamic recovery process [26]. However, ε_p decreases from 0.438 to 0.339 with the Ga content from 1 to 2% and further decreases with the Ga content from 3 to 5%, which is related to the onset of DRX.

The critical strain of DRX is an important indicator for the onset of DRX and the flow stress curve cannot directly reflect the critical strain value. Poliak et al. [31] show that the θ – σ curve ($\theta = \partial\sigma / \partial\varepsilon$, where σ is the true stress and ε is the true strain) of the material exhibits the inflection point characteristic when DRX occurs. The inflection point corresponds to the minimum value of the $-\partial\theta/\partial\sigma$ – σ curve, the stress corresponding to the minimum value is the critical stress (σ_c) of DRX and the corresponding strain value is the critical strain (ε_c).

The θ – σ and $-(\partial\theta/\partial\sigma)$ – σ curves of the Mg–Ga alloys are shown in Fig. 7b and c. σ_c is obtained from Fig. 7b and c, while the corresponding ε_c is achieved from Fig. 7a. The variations in σ_c and ε_c with respect to the Ga content are shown in Table 3. As compared with Table 2, σ_c and ε_c of each alloy are smaller than the corresponding σ_p and ε_p , indicating that DRX occurs before the peak stress. As far as ε_c is concerned, it decreases at first and then increases with the higher Ga content. It is worth noting that ε_c of the Mg–1 Ga alloy is the largest and that of the Mg–2 Ga alloy is the smallest among all the alloys, indicating that the increase of the Ga content can promote the DRX process. ε_c of the alloy increases from 0.266 to 0.281 with the Ga content from 2 to 5%, indicating that the higher Ga content retards DRX. The hot compression results are consistent with the as-rolled microstructure evolutions.

3.4 Mechanical Properties and Anisotropy

The typical tensile stress–strain curves of the as-rolled Mg–Ga alloys are shown in Fig. 8. The mechanical properties are listed in Table 4. The Mg–1 Ga alloy exhibits σ_b of 249 MPa, $\sigma_{0.2}$ of 211 MPa and δ of 21.2%. With the higher Ga content, σ_b increases monotonically, while $\sigma_{0.2}$ decreases at first and then increases. The Mg–3 Ga alloy has the lowest $\sigma_{0.2}$ of 196 MPa, while the Mg–5 Ga alloy exhibits the highest σ_b of 292 MPa. All the alloys exhibit relatively high δ values at room temperature. With the Ga content increasing, δ of the alloy increases at first and then decreases. The as-rolled Mg–2 Ga alloy exhibits an ultra-high plasticity, with δ high up to 36.6%.

The comparison of the room temperature mechanical properties of some magnesium alloy sheets under the similar tensile strain rates is displayed in Table 5. The as-HSRRed Mg–Ga alloys exhibit the slightly lower σ_b values than those of the traditional commercial magnesium alloys such as AZ31 [32], ZK60 [33], but they have similar yield strength and obviously higher elongation. At the same time, the Ga addition makes the alloy sheet have better mechanical properties than the other alloying elements such as Sn [34], Li [35], Zn [35]. Moreover, the Mg–Ga alloys have comparable or even better mechanical properties than some Mg–RE alloys [36, 37]. Evidently, the as-HSRRed Mg–Ga alloys have outstanding mechanical properties with high plasticity.

Table 3 The critical stress and the critical strain of the Mg–Ga alloys

Ga content (mass%)	Critical stress σ_c (MPa)	Critical strain ε_c
1	107	0.304
2	129	0.266
3	138	0.271
5	126	0.281

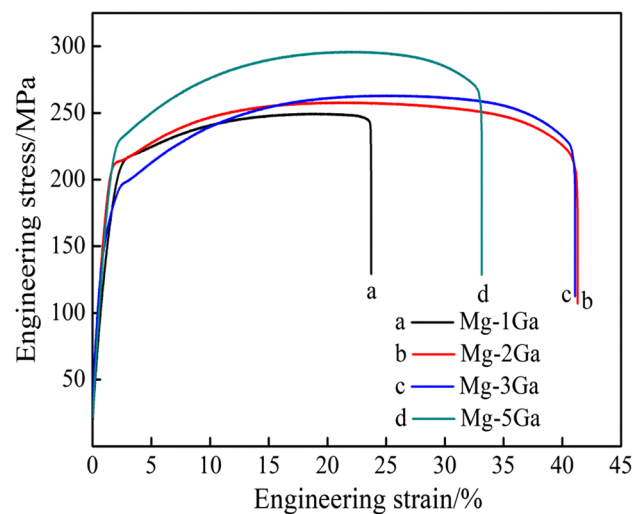


Fig. 8 The typical stress–strain curves of the as-rolled Mg–Ga alloys

SEM tensile fracture images of the as-rolled Mg–Ga alloys are shown in Fig. 9. All the fracture surfaces consist of a large number of uniform dimples and tearing edges, showing a typical ductile fracture. As seen from Fig. 9b–d, the Mg–2 Ga and Mg–3 Ga alloys have more deep dimples than the Mg–5 Ga alloy. As shown in Fig. 9a, the Mg–1 Ga alloy has some dimples and cleavage facets. As shown in Fig. 9c and d, there are some broken particles in the centers of the dimples in the alloys with 3%Ga or higher. The secondary phase particles are extremely small in the Mg–3 Ga alloy, while those in the Mg–5 Ga alloy are around 2 μm . As shown in Fig. 10, the secondary phase particles in the Mg–5 Ga alloy are featured with a high Ga content and are considered to be Mg_5Ga_2 .

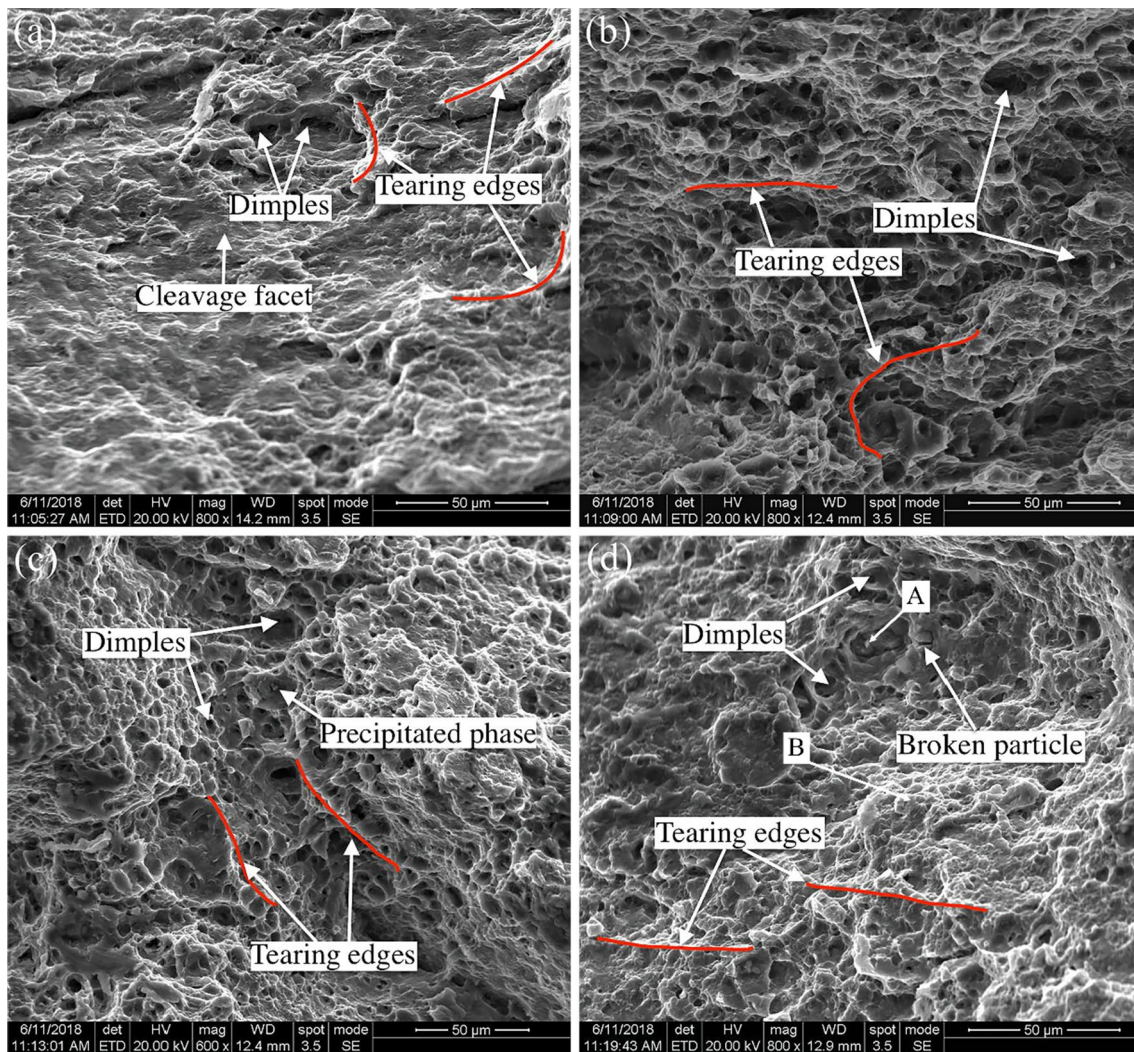
Anisotropy means that the properties of materials change with the testing direction, while isotropy means that the properties of materials are independent of the testing direction. Specifically, mechanical anisotropy means mechanical properties of materials including tensile strength, yield strength and elongation to rupture change with the testing direction. The Mg–2 Ga alloy sheet is selected to further characterize the mechanical anisotropy of the HSRRed

Table 4 Mechanical properties of the as-rolled Mg–Ga alloys

Ga content (mass%)	Sample direction	σ_b (MPa)	$\sigma_{0.2}$ (MPa)	δ (%)
1	RD	249	211	21.2
2	RD	258	213	36.6
	RD-45°	239	188	33.5
	TD	240	200	33.8
3	RD	263	196	33.9
5	RD	292	230	30.3

Table 5 Comparison of mechanical properties of magnesium alloy sheets at room temperature

Materials	State	Tensile strain rate (s^{-1})	$\sigma_{0.2}$ (MPa)	σ_b (MPa)	δ (%)	References
AZ31	As-rolled	1.0×10^{-3}	190	271	17.9	[32]
ZK60	As-rolled	0.67×10^{-3}	220	326	19.5	[33]
Mg–9Al–1Zn–0.4Sn	As-rolled	1.0×10^{-3}	201	291	9.1	[34]
Mg–4Li	As-extruded	1.0×10^{-3}	105	163	16.5	[35]
Mg–4Li–6Zn–1.2Y			141	240	21.6	
Mg–2Zn–0.2Ce	As-extruded	1.0×10^{-3}	135	225	27	[36]
Mg–5Zn–0.2Ce			135	247	15	
Mg–1Y	As-extruded	1.0×10^{-3}	104	181	35.2	[37]
Mg–5Y			173	214	22.8	
Mg–2 Ga	HSRR	1.1×10^{-3}	213	258	36.6	This work
Mg–5 Ga	HSRR	1.1×10^{-3}	230	292	30.3	This work

**Fig. 9** SEM tensile fracture images of as-rolled **a** Mg–1 Ga, **b** Mg–2 Ga, **c** Mg–3 Ga, and **d** Mg–5 Ga alloys

Mg–Ga alloy sheet in the present study. Mechanical properties of the HSRRed Mg–2 Ga alloy sheet in rolling direction (RD), 45° to rolling direction (RD-45°) and transverse

direction (TD) are listed in Table 4. It can be seen that yield strength and elongation to rupture in the three testing directions exhibit only slight differences.

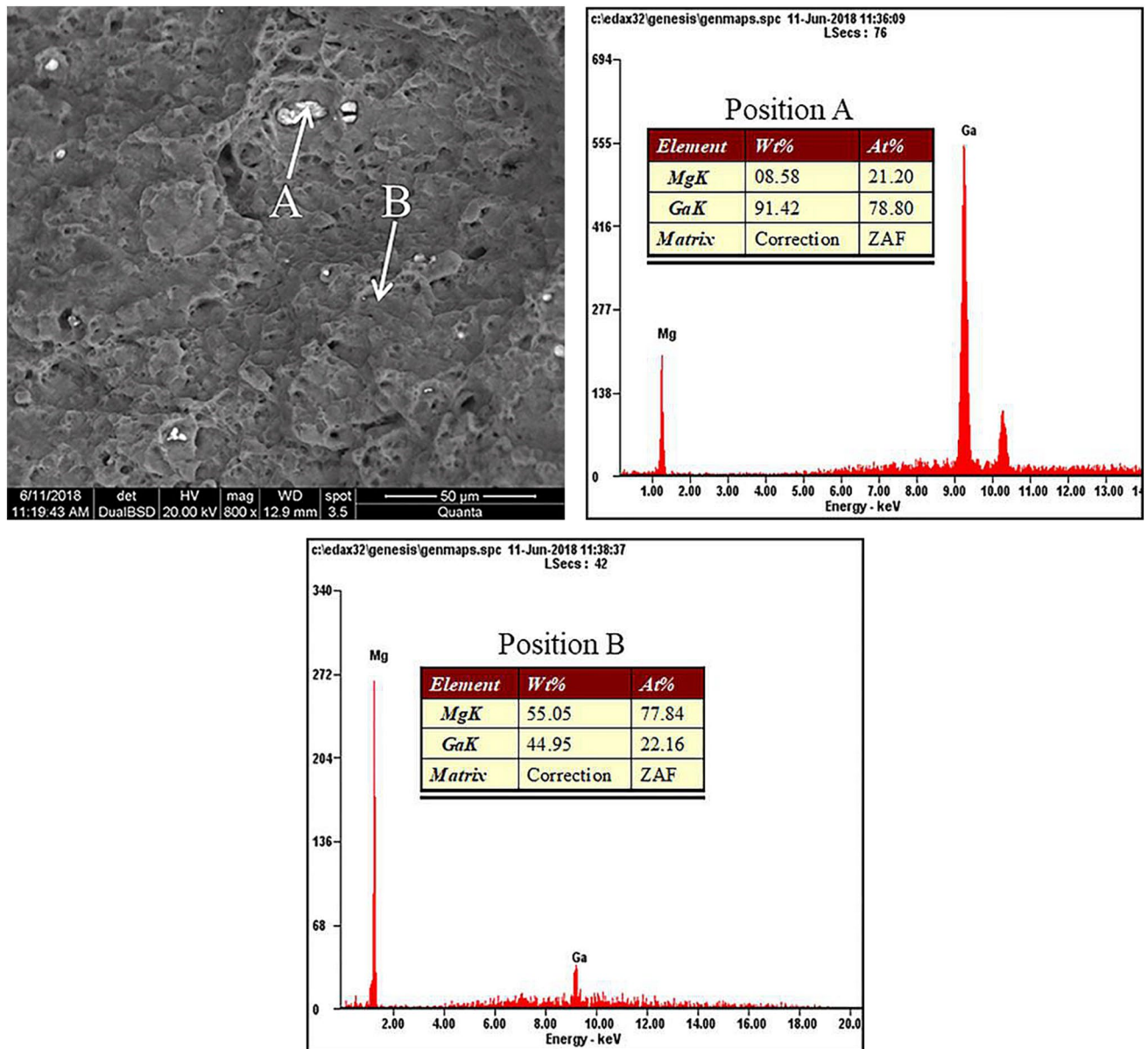


Fig. 10 EDS results of the positions in Fig. 9d

The in-plane anisotropy (*IPA*) is adopted to evaluate the mechanical anisotropy of the alloy sheet [38]. The *IPA* value of yield strength can be expressed as Eq. (1). Generally, the yield strength along RD is the highest. The *IPA* value of the HSRRed Mg–2 Ga alloy is 8.9%. However, the *IPA* values of the as-extruded Mg–2Zn–0.5RE alloy sheet [39], the as-rolled AZ31–0.5Ca alloy sheet [40], the as-rolled Mg–9Al–1Zn–0.4Sn alloy sheet [34] and the as-extruded ZK60 alloy sheet [41] are 10%, 10.2%, 17.3% and 34.5%, respectively. Obviously, the HSRRed Mg–2 Ga alloy exhibits relatively low yield strength anisotropy.

$$IPA = [2\sigma_s(RD) - \sigma_s(RD - 45^\circ) - \sigma_s(TD)] / 2\sigma_s(RD) \quad (1)$$

Moreover, the plasticity anisotropy is not visible since the elongations to rupture of the Mg–2 Ga alloy in the three testing directions are similar. In comparison with the as-extruded Mg–2Zn–0.5Ca and Mg–2Zn–0.5RE alloy sheets [39], the as-extruded ZK60 alloy sheet [41] and the as-rolled Mg–9Al–1Zn–0.4Sn alloy sheet [34], the HSRRed Mg–2 Ga alloy exhibits much lower plasticity anisotropy, which is beneficial to the subsequent punching forming.

4 Discussion

On the basis of microstructure evolutions, the DRX critical strain and mechanical properties of the Mg–Ga alloys, it can be concluded that the Ga content plays an extremely important role in the HSRRed Mg alloy sheets. Effects of Ga content on microstructure evolutions and mechanical properties of the Mg–Ga alloys are further discussed as the following.

4.1 Effects of Ga Content on DRX During High Strain Rate Deformation

As shown in Fig. 4 and Table 3, the Mg–2 Ga alloy has the highest DRX volume fraction (98%) and the smallest critical strain for DRX. In the other words, the 2%Ga addition is beneficial to the enhanced DRX process. The reason for this phenomenon is possibly related to the DRX mechanism. Twin-aided DRX (TDRX) [42–44] is one of the mechanisms for plastic deformation of Mg alloys. It is reported that this mechanism would occur in Mg alloys when the local stress at the twin boundary exceeds the critical resolved shear stress (CRSS) for the (c + a) dislocation slip [45, 46].

In recent years, twinning attracts more attentions in connection with DRX of Mg alloys [47, 48]. Zhu et al. [48] have proposed that high strain rate deformation induces a high number density of twins, including a predominance of {10–11}–{10–12} double twins in coarse grains, a predominance of {10–12} twins in fine DRX grains and a new observation of {10–12} nano twins in ultrafine grains with high density in bulky Mg alloys. The high trend for twinning at high strain rates offers the nucleation sites for DRX, resulting in a uniform, ultrafine-grained microstructure which exhibits a weakened basal texture and thus excellent mechanical properties. Wu et al. have found that the introduction of twins through pre-deformation before high strain rate rolling can facilitate DRX, which significantly increases the strength of ZM61 alloy [49]. Thus, it can be concluded the more the deformation twins generated during the HSRR process, the more the nucleation sites for DRX are. Therefore, effects of the Ga addition on the DRX of Mg alloys can be attributed to the influence of the Ga addition on twinning during the deformation process.

Grain size has an important impact on twinning during plastic deformation [50]. The larger the grain size, the more likely the twins will occur. As shown in Fig. 1, the grain size decreases with the higher Ga content, indicating that an increase in the Ga content would hinder the DRX process. However, the result shown in Figs. 3 or 5 is just the opposite. Therefore, the other factors affecting DRX should be considered. According to Eq. (2) [51]:

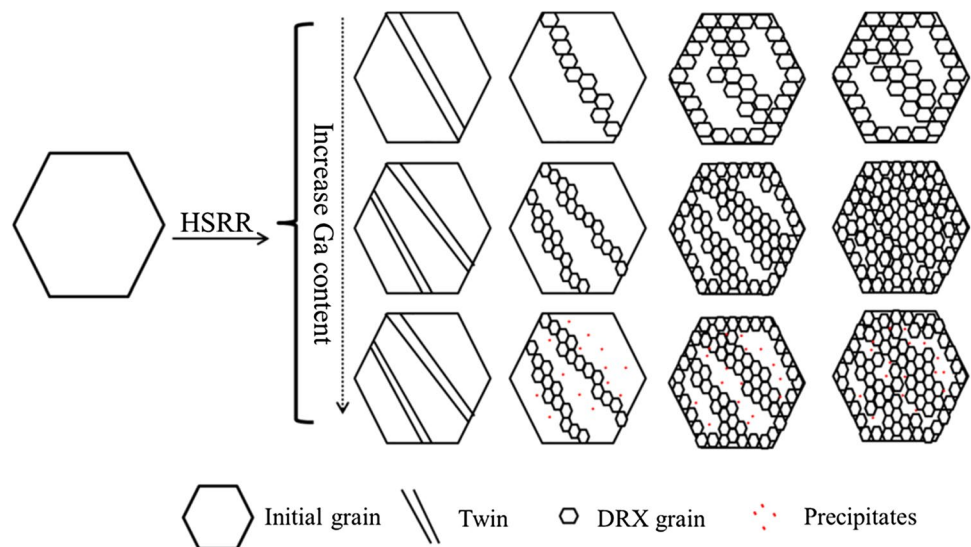
$$\sigma^2 = \frac{5\pi}{2} \cdot \frac{\rho G \gamma_{TB}}{\lambda_C} \quad (2)$$

where σ is the driving force for twin formation related to twin boundary energy (γ_{TB}), G is the shear modulus, ρ is the ratio of thickness to diameter of the twin embryo and λ_C is the critical twin nucleus thickness. SFE decreases dramatically and the driving force for twin nucleation decreases since γ_{TB} is proportional to SFE, Therefore, stacking fault energy (SFE) is an important factor affecting the twinning behavior. The twinning density is generally found to be higher in the alloy with a low SFE [52–55]. Twinning becomes the dominant deformation mechanism in the alloys with low SFE and can be obviously enhanced by decreasing the SFE [56, 57]. According to the references [27–29], the Ga addition can significantly reduce the SFE of Mg alloys. Therefore, the DRX critical strains corresponding to the Mg–2 Ga, Mg–3 Ga and Mg–5 Ga alloys are smaller than that of the Mg–1 Ga alloy, which can be attributed to the reduced SFE effect by Ga addition.

Moreover, the reduced SFE can also explain that the Mg–1 Ga alloy exhibits the smaller DRX volume fraction than the other alloys. As shown in Figs. 3, 4 and Table 3, the DRX volume fraction decreases and the critical strain of DRX increases with the Ga content higher than 2%, indicating a further increase in the Ga content inhibits the DRX process to some extent. Dynamic precipitates appear to be ubiquitous during hot deformation. During the high strain rate deformation, the high-density dislocations can offer the diffusion channels for solute atoms and thus accelerate the enrichment rate of solute atoms. In addition, the existence of dislocations can provide the driving force for precipitation, which can induce the nucleation of dynamic precipitates. According to the Ref. [8], the large secondary phase particles ($> 1 \mu\text{m}$) can promote DRX by the particle stimulate nucleation (PSN) mechanism [9, 57], while the dispersed small secondary phase particles can hinder DRX by the pinning dislocations (Zener resistance). As seen from Fig. 6, the visible Mg_5Ga_2 diffraction peaks are detected in the as-rolled Mg–5 Ga alloy. As compared with Fig. 2, it is clear that the Mg_5Ga_2 phase is precipitated from the matrix and the diffraction peak intensities corresponding to the Mg_5Ga_2 phase increase with the higher Ga content. In other words, more Mg_5Ga_2 dynamic precipitates are precipitated in the alloy with a higher Ga content. Therefore, the reduced DRX degree can be attributed to the hindrance of the dynamic precipitates in the alloy with 2%Ga or higher. The similar phenomena have also been reported in the Ref. [42, 58].

The sketch map of microstructure evolution of Mg–Ga alloy during high strain rate rolling is shown in Fig. 11. Solute Ga atoms increase the density of twins during the deformation process, which can provide the nucleation sites for recrystallization, thus promoting the process of DRX and finally obtaining the fine and uniform microstructure. At the same time, excessive solute Ga atoms are easy to be precipitated out of the matrix in the form of the secondary phase

Fig. 11 The sketch map of microstructure evolution of the Mg–Ga alloy during high strain rate rolling



particles during the deformation process, which can inhibit or delay the DRX. Therefore, the hot-deformed microstructure can be controlled by properly adjusting the content of alloying elements, which can meet the actual requirements.

However, only a slight increase in the DRX volume fraction is observed in the surface-layer microstructure of the Mg–5 Ga alloy and the detailed reason should be further considered. As shown in Figs. 5 and 9, both the number density and the size of the precipitates in the Mg–5 Ga alloy are bigger than the counterparts in the other alloys. As shown in Fig. 9d, the secondary phase particles with the size around 2 μm are detected in the HSRRed Mg–5 Ga alloy, which are possibly the reason for the slight increase in the DRX volume fraction since the PSN mechanism is involved.

4.2 Effects of Ga Content on Mechanical Properties of the HSRRed Mg–Ga Alloys

Generally, the strengthening mechanisms for wrought Mg alloys include grain refinement strengthening, precipitation strengthening, solid solution strengthening and dislocation strengthening. A possible expression of yield strength is approximated linearly as Eq. (3) [59].

$$\sigma_y = \Delta\sigma_{gb} + M(\tau_0 + \Delta\tau_p + \Delta\tau_s + \Delta\tau_d) \quad (3)$$

where σ_y is yield strength, $\Delta\sigma_{gb}$ is the grain refinement strengthening, M is the Taylor factor, τ_0 is the intrinsic critical resolved shear stress, $\Delta\tau_p$, $\Delta\tau_s$, and $\Delta\tau_d$ are precipitation strengthening, solid solution strengthening and dislocations strengthening, respectively. As seen from Fig. 8 and Table 4, the solid solution strengthening caused by the increased Ga content fails to compensate for the strength drop caused by the bigger grain size and thus the Mg–3 Ga alloy exhibits lower yield strength than the Mg–1 Ga and Mg–2 Ga alloys. Therefore, the factors affecting the strength of Mg–Ga

alloys mainly include grain size, precipitates and dislocation density.

According to the Hall–Petch relation [60] $\sigma = \sigma_0 + kd^{-1/2}$ (where σ_0 is the internal frictional stress, k is the Hall–Petch constant, and d is the grain size), it can be seen that the yield strength is reduced with a bigger grain size. As shown in Fig. 4, the grain size of the Mg–3 Ga alloy is the biggest among the four alloys and thus its yield strength is the lowest. The grain sizes of the Mg–1 Ga and Mg–2 Ga alloys are similar and the Mg–1 Ga alloy exhibits comparable yield strength to the Mg–2 Ga alloy. The latter is associated with the absence of the un-DRX regions in the Mg–2 Ga alloy. Except for the grain refinement strengthening, precipitation strengthening has a strong strengthening effect. According to the Orowan mechanism [61], the precipitates can improve the strength of the alloys and more Mg_5Ga_2 particles are existent in the Mg–5 Ga alloy, which contribute to its highest yield strength.

The plasticity of wrought alloys is tightly related to their microstructure. Generally, the higher the DRX volume fraction is, the better the plasticity is. As shown in Table 4, the Mg–1 Ga alloy has the lowest δ , while the Mg–2 Ga alloy exhibits the highest δ . As shown in Fig. 9, the SEM tensile fracture images of the as-rolled Mg–Ga alloys consist of a large number of uniform dimples and tearing edges, showing a typical ductile fracture. The Mg–2 Ga and Mg–3 Ga alloys exhibit a large number of deeper dimples, indicating their good plasticity. In addition, the presence of coarse precipitates would seriously reduce the plasticity of the alloy. As seen from Fig. 9c and d, some broken Mg_5Ga_2 particles are existent at the center of the dimples in the alloy with a higher Ga content. As stated above, the hard Mg_5Ga_2 particles can hinder the movement of dislocations, causing the pile-up of dislocations during the plastic deformation and thus brings about

the strength enhancement. However, these particles would become the crack initiation sources and lead to crack propagation during the tensile testing, resulting in the relatively low plasticity of the Mg–5 Ga alloy.

As stated above, the HSRRed Mg–2 Ga alloy sheet exhibits the relatively low yield strength anisotropy and the slight plasticity anisotropy, which are beneficial to the subsequent punching forming. Moreover, the HSRRed Mg–2 Ga alloy exhibits an ultra-high plasticity (with the elongation to rupture of 36.6%). It is possibly related to the complete DRX. In fact, the Ga addition plays an important role on the mechanical anisotropy of the HSRRed Mg–Ga alloy sheets. The related mechanisms are being further studied. Due to the length limitations, this part of the study will be reported in the other paper.

5 Conclusions

In the present work, effects of Ga content on microstructure, DRX and mechanical properties of the Mg–Ga alloys prepared by HSRR are carefully investigated. The main conclusions are drawn as the following.

- (1) Ga can promote DRX by reducing the stacking fault energy and increasing the number of twins, while twins are the nucleation sites for DRX. The Mg–1 Ga alloy exhibits the biggest DRX critical strain of 0.304 among all the alloys.
- (2) Fine dynamic precipitates can hinder DRX by pinning dislocations and inhibiting the grain boundary migration, but the larger-size precipitates can promote DRX through the PSN mechanism in the as-rolled Mg–5 Ga alloy.
- (3) The HSRRed Mg–2 Ga alloy exhibits an ultra-high plasticity (with δ around 36.6%) and a relatively low anisotropy of yield strength and plasticity, due to the complete DRX. The HSRRed Mg–5 Ga alloy exhibits the best comprehensive mechanical properties, with σ_b of 292 MPa, $\sigma_{0.2}$ of 230 MPa and δ of 30.3%, due to precipitation strengthening and grain refinement strengthening.

Acknowledgements This work is supported by National Natural Science Foundation of China (Grant Nos. 51571089 and 51871093).

Compliance with Ethical Standards

Conflict of interest The authors declare that they have no conflict of interest.

References

1. J. Hirsch, T. Al-Samman, *Acta Mater.* **61**, 818–843 (2013)
2. B.L. Mordike, *Mater. Sci. Eng. A* **302**, 37–45 (2001)
3. A.A. Luo, N.R. Neelameggham, *Materials comparison and potential applications of magnesium in automobiles*. In: *Essential Readings in Magnesium Technology*, (Springer, Berlin, 2016), pp. 25–34
4. K. Hono, C.L. Mendis, T.T. Sasaki, *Scr. Mater.* **63**, 710–715 (2010)
5. A.R. Antoniswamy, E.M. Taleff, L.H. Jr, J.T. Carter, *Mater. Sci. Eng. A* **631**, 1–9 (2015)
6. D. Raabe, *Recovery and recrystallization: phenomena, physics, models, simulation*, in *Physical Metallurgy*, (Elsevier, Germany, 2014), pp. 2291–2397
7. Y.V.R.K. Prasad, N. Ravichandran, *Bull. Mater. Sci.* **14**, 1241–1248 (1991)
8. D.L. Holt, *Acta Metall.* **13**, 39–40 (1965)
9. R.D. Doherty, D.A. Hughes, F.J. Humphreys, J.J. Jonas, D.J. Jensen, M.E. Kassner, W.E. King, T.R. McNelley, H.J. McQueen, A.D. Rollett, *Mater. Sci. Eng. A* **238**(2), 219–274 (1997)
10. M. Hradilová, F. Montheillet, A. Fraczkiewicz, C. Desrayaud, P. Lejček, *Mater. Sci. Eng. A* **579**, 209–216 (2013)
11. R.P. Beck, *Recl. Trav. Chim. Pays-Bas* **41**, 353–399 (1922)
12. A.A. Nayeb-Hashemi, J.B. Clark, *Bull. Alloy Phase Diagr.* **6**, 434–439 (1985)
13. Y.B. Kang, J. Jeong, H.O. Sang, *Comput. Coupling Phase Diagr. Thermochem.* **46**, 168–175 (2014)
14. Q. Gao, Y. Du, D. Zhao, A. Wang, J. Wang, S. Liu, Y. Ouyang, *Comput. Coupling Phase Diagr. Thermochem.* **37**, 137–144 (2012)
15. J. Zhao, K. Yu, Y. Hu, S. Li, X. Tan, F. Chen, Z. Yu, *Electrochim. Acta* **56**, 8224–8231 (2011)
16. Y. Geng, R. Wang, C. Peng, *Trans. Nonferrous Met. Soc. China* **23**, 2650–2656 (2013)
17. Y. Feng, R.C. Wang, C.Q. Peng, *Corrosion* **67**, 1–6 (2011)
18. D. Wu, L. Ouyang, C. Wu, H. Wang, J. Liu, L. Sun, M. Zhu, *J. Alloys Compd.* **642**, 180–184 (2015)
19. D.O. Flamini, S.B. Saidman, J.B. Bessone, *Corros. Sci.* **48**, 1413–1425 (2006)
20. Y. Feng, R. Wang, K. Yu, C. Peng, J. Zhang, C. Zhang, *J. Alloys Compd.* **473**, 215–219 (2009)
21. Y. Feng, R.C. Wang, C.Q. Peng, N. Wang, *Trans. Nonferrous Met. Soc. China* **19**, 154–159 (2009)
22. Y. Feng, R.C. Wang, C.Q. Peng, H.P. Tang, H.Y. Liu, *Prog. Nat. Sci. Mater. Int.* **21**, 73–79 (2011)
23. M. Mohedano, C. Blawert, K.A. Yasakau, R. Arrabal, E. Matykina, B. Mingo, N. Scharnagl, M.G. Ferreira, M.L. Zheludkevich, *Mater. Charact.* **128**, 85–99 (2017)
24. J. Kubásek, D. Vojtěch, D. Dvorský, *Int. J. Mater. Res.* **107**, 459–471 (2016)
25. J. Kubásek, D. Vojtěch, J. Lipov, T. Ruml, *Mater. Sci. Eng. C* **33**, 2421–2432 (2013)
26. H.B. Liu, G.H. Qi, Y.T. Ma, H. Hao, F. Jia, S.H. Ji, H.Y. Zhang, X.G. Zhang, *Mater. Sci. Eng. A* **526**, 7–10 (2009)
27. Q. Dong, Z. Luo, H. Zhu, L.Y. Wang, T. Ying, Z.H. Jin, D.J. Li, W.J. Ding, X.Q. Zeng, *J. Mater. Sci. Technol.* **34**, 1773–1780 (2018)
28. C. Wang, H.Y. Zhang, H.Y. Wang, G.J. Liu, Q.C. Jiang, *Scr. Mater.* **69**, 445–448 (2013)
29. J. Zhang, Y.C. Dou, G.B. Liu, Z.X. Guo, *Comput. Mater. Sci.* **79**, 564–569 (2013)
30. S.Q. Zhu, H.G. Yan, J.H. Chen, Y.Z. Wu, J.Z. Liu, J. Tian, *Scr. Mater.* **63**, 985–988 (2010)
31. E.I. Poliak, J.J. Jonas, *Acta Mater.* **44**, 127–136 (1996)

32. X. Rao, Y. Wu, X. Pei, Y. Jing, L. Luo, Y. Liu, J. Lu, *Mater. Sci. Eng. A* **754**, 112–120 (2019)
33. W. Wang, L. Ma, S. Chai, W. Zhang, W. Chen, Y. Feng, G. Cui, *Mater. Sci. Eng. A* **730**, 162–167 (2018)
34. Z.P. Yu, Y.H. Yan, J. Yao, C. Wang, M. Zha, X.Y. Xu, Y. Liu, H.Y. Wang, Q.C. Jiang, *J. Alloys Compd.* **744**, 211–219 (2018)
35. C.Q. Li, D.K. Xu, S. Yu, L.Y. Sheng, E.H. Han, *J. Mater. Sci. Technol.* **33**, 475–480 (2018)
36. A.A. Luo, R.K. Mishra, A.K. Sachdev, *Scr. Mater.* **64**, 410–413 (2011)
37. G.H. Huang, D.D. Yin, J.W. Lu, H. Zhou, Y. Zeng, G.F. Quan, Q.D. Wang, *Mater. Sci. Eng. A* **720**, 24–35 (2018)
38. K.V. Jata, A.K. Hopkins, R.J. Rioja, *Mater. Sci. Forum* **217–222**, 647–652 (1996)
39. M. Mabuchi, K. Higashi, *Acta Mater.* **44**, 4611–4618 (1996)
40. U.M. Chaudry, Y.S. Kim, K. Hamad, *Mater. Lett.* **238**, 305–308 (2019)
41. H.Y. Wang, J. Rong, Z.Y. Yu, M. Zha, C. Wang, Z.Z. Yang, R.Y. Bu, Q.C. Jiang, *Mater. Sci. Eng. A* **697**, 149–157 (2017)
42. S.W. Xu, S. Kamado, N. Matsumoto, T. Honma, Y. Kojima, *Mater. Sci. Eng. A* **527**, 52–60 (2009)
43. S.Q. Zhu, S.P. Ringer, *Acta Mater.* **144**, 365–375 (2018)
44. O. Sitdikov, R. Kaibyshev, *Mater. Trans.* **42**, 1928–1937 (2001)
45. H.P. Chan, C.S. Oh, S. Kim, *Mater. Sci. Eng. A* **542**, 127–139 (2012)
46. G. Aggarwal, *Acta Mater.* **49**, 1199–1207 (2001)
47. O. Sitdikov, R. Kaibyshev, *Mater. Trans.* **42**, 1928–1937 (2001)
48. S.Q. Zhu, H.G. Yan, X.Z. Liao, S.J. Moody, G. Sha, Y.Z. Wu, S.P. Ringer, *Acta Mater.* **82**, 344–355 (2015)
49. J. Wu, J. Chen, H. Yan, X.W. Xia, B. Su, L. Yu, G.S. Liu, M. Song, *J. Mater. Sci.* **52**, 1–10 (2017)
50. A. Ghaderi, M.R. Barnett, *Acta Mater.* **59**, 7824–7839 (2011)
51. M.A. Meyers, O. Vöhringer, V.A. Lubarda, *Acta Mater.* **49**, 4025–4039 (2001)
52. H.T. Wang, N.R. Tao, K. Lu, *Acta Mater.* **60**, 4027–4040 (2012)
53. Y. Zhang, N.R. Tao, K. Lu, *Acta Mater.* **59**, 6048–6058 (2011)
54. D.C. Bufford, Y.M. Wang, Y. Liu, *MRS Bull.* **41**, 286–291 (2016)
55. J.P. Liebig, S. Krauß, M. Göken, B. Merle, *Acta Mater.* **154**, 261–272 (2018)
56. I.J. Beyerlein, X. Zhang, A. Misra, *Annu. Rev. Mater. Sci.* **44**, 329–363 (2014)
57. Z.W. Yu, A.T. Tang, J.J. He, Z.Y. Gao, J. She, J.G. Liu, F.S. Pan, *Mater. Charact.* **136**, 310–317 (2018)
58. C. Chen, J. Chen, H. Yan, B. Su, M. Song, S.Q. Zhu, *Mater. Des.* **100**, 58–66 (2016)
59. L.F. Wang, E. Mostaed, X.Q. Cao, G.S. Huang, A. Fabrizi, F. Bonollo, C.Z. Chi, M. Vedani, *Mater. Des.* **89**, 1–8 (2016)
60. M.J. Starink, S.C. Wang, *Acta Mater.* **51**, 5131–5150 (2003)
61. H. Ding, X. Shi, Y. Wang, G. Cheng, S. Kamado, *Mater. Sci. Eng. A* **645**, 196–204 (2015)

Publisher's Note Springer Nature remains neutral with regard to jurisdictional claims in published maps and institutional affiliations.